Available at www.sciencedirect.com

ScienceDirect

journal homepage: www.elsevier.com/locate/he

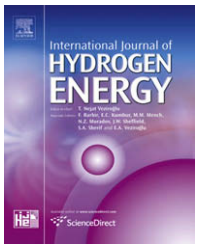

Configuration effects of air, fuel, and coolant inlets on the performance of a proton exchange membrane fuel cell for automotive applications

Sanggyu Kang[a], *Kyoungdoug Min*[a,*], *Fabian Mueller*[b], *Jacob Brouwer*[b]

[a]*School of Mechanical and Aerospace Engineering, Seoul National University, Seoul 151-742, Republic of Korea*
[b]*Mechanical and Aerospace Engineering Department, National Fuel Cell Research Center, University of California, Irvine, USA*

ARTICLE INFO

Article history:
Received 10 February 2009
Received in revised form
6 June 2009
Accepted 13 June 2009
Available online 15 July 2009

Keywords:
Flow configuration
Fuel flow direction
Air flow direction
Coolant flow direction
PEMFC

ABSTRACT

The configuration of fuel, air, and cooling water paths is one of the major factors that influence the performance of a proton exchange membrane fuel cell (PEMFC). In order to investigate the effects of these factors, a quasi-three-dimensional dynamic model of a PEMFC has been developed. For validation, simulation results are compared with experimental data in one-flow configuration case and show good agreement with the experimental cell performance data. Five different flow configurations are then simulated to systematically investigate the effects of fuel, air, and cooling channel configuration on the local current and species distribution. Voltage and power vs. current density for five different configurations are compared. The type 1 configuration, which has a fuel–air counter flow and an air-coolant co-flow, has the highest performance in all ranges of current density because the membrane remains the most hydrated. When the operating current density increases, the effects of temperature on membrane hydration slightly decrease. It is confirmed that fuel cell performance improves with increased humidity until flooding conditions appear. An interesting result shows that it is possible to lower the fuel cell operating temperature to improve fuel cell hydration, which in turn improves cell performance. In addition, the different flow configurations are shown to have an effect on the pressure losses and local current density, membrane hydration, and species mole fractions. These results suggest that the model can be used to optimize the flow configuration of a PEMFC.

1. Introduction

The proton exchange membrane fuel cell (PEMFC) is a promising future power source for vehicles, materials handling equipment, and backup and portable power applications. PEMFCs have relatively high efficiencies, high power density, low temperature operation, quick start-up, system robustness, transient ability, and low emissions features [1–3]. These features of PEMFC systems make them attractive as future automobile power sources.

In the present research, a methodology that uses a quasi-three-dimensional model to determine optimal flow configuration and operating parameters was developed. Fuel, air and coolant flow directions all concurrently affect PEMFC performance, and each must therefore be analyzed. In addition to the fuel and air, which directly affect fuel cell

* *Corresponding author*. Tel.: +82 2 880 1661.
E-mail address: kdmin@snu.ac.kr (K. Min).

0360-3199/$ – see front matter © 2009 International Association for Hydrogen Energy. Published by Elsevier Ltd. All rights reserved.
doi:10.1016/j.ijhydene.2009.06.049

Nomenclature

A	surface area, m^2
a	Water activity, –
a_c	activation polarization coefficient, –
C	solid specific heat capacity, $kJ\,kg^{-1}\,K^{-1}$
$\vec{C}$	species molar concentration (H_2, H_2O, N_2, O_2), $kmol\,m^{-3}$
C_V	constant volume gas specific heat capacity, $kJ\,kg^{-1}\,K^{-1}$
C_P	constant pressure gas specific heat capacity, $kJ\,kg^{-1}\,K^{-1}$
$\vec{D}$	diffusion coefficient, $m^2\,s^{-1}$
D_H	hydraulic diameter, m
F	Faraday's constant, 96,487 $C\,mol^{-1}$
$\vec{g}_m$	mass transport coefficient, $m\,s^{-1}$
ΔG	change of Gibbs free energy, $kJ\,mol^{-1}$
h	enthalpy, $kJ\,kmol^{-1}$, convective heat transfer coefficient, $kW\,m^{-2}\,K^{-1}$
ΔH	enthalpy of formation, $kJ\,mol^{-1}$
I	electrical current, A
i_o	exchange current density, $A\,m^{-2}$
k_f	fluid conduction heat transfer coefficient, $kW\,m^{-1}\,K^{-1}$
k_s	solid conduction heat transfer coefficient, $kW\,m^{-1}\,K^{-1}$
L	length, m
N	molar capacity, or total number of moles, kmol
$\vec{N}$	species molar capacity, kmol
$\dot{N}$	molar flow rate, $kmol\,sec^{-1}$
n	number of participating electrons in the reaction, –
n_d	osmotic drag coefficient, –
Nu_D	Nusselt number, –
P	pressure, Kpa
$\dot{Q}$	heat transfer, kW
R	universal gas constant, $8.3145\,kJ\,kmol^{-1}\,K^{-1}$; fuel cell external/load resistance, ohm
$\vec{R}$	Species reaction rate (H_2, H_2O, N_2, O_2), $kmol\,s^{-1}$
Sh	Sherwood number, –
T	temperature, K
t	Time, s; thickness, m
V	voltage, V
$\forall$	volume, m^3
$\vec{X}$	species mole fraction (H_2, H_2O, N_2, O_2), –
x	spatial distance, m
$\dot{m}$	mass flow rate, kgs^{-1}
v	fluid velocity, ms^{-1}
g	gravity acceleration, ms^{-2}
f	friction factor, –
hm	head loss, –
K	loss coefficient, –

Greek letters

ε	porosity of GDL, –
$\vec{\Phi}$	species diffusion flux between GDL and bulk gases (H_2, H_2O, N_2, O_2), $kmol\,s^{-1}$
Ψ_{H_2O}	water diffusion flux between GDL and MEA, $kmol\,s^{-1}$
Θ_{H_2O}	water osmotic flux through the MEA, $kmol\,s^{-1}$
ρ	density of solid, $kg\,m^{-2}$
λ	membrane hydration, –
μ	viscosity, $kgm^{-1}\,s^{-1}$
η_v	volumetric efficiency, –
η_m	mechanical efficiency, –
η_h	hydraulic efficiency, –

Subscripts

act	activation polarization
gdl	gas diffusion layer
in	into control volume
m	membrane dry basis
mea	membrane electrolyte assembly
mem	membrane
o	standard condition
ohm	Ohmic polarization
out	out of control volume
sat	water saturation

electrochemistry, it is important to consider the coolant flow configuration as well. Since the active area of fuel cells for automotive applications is relatively large, it affects performance; thus, performance depends significantly upon the coolant configuration.

In order to determine the factors that affect the performance of a PEMFC and to investigate the actual effects of these factors, various models have been developed. The models are often used to reduce development costs, accelerate design cycle times, and improve performance. Springer et al. [4] developed one of the first models of a PEMFC. They experimentally determined the diffusion and electro-osmotic drag coefficients of water in Nafion 117® that were first used to predict the steady-state, one-dimensional water profile and the resulting proton conductivity in a PEMFC. Bernardi et al. [5] developed their model more extensively by considering the multiple electrochemical reactions and transport phenomena in the computational domain. They also investigated the electro-kinetic effect and the effect of ohmic resistance on the performance of a PEMFC. The one-dimensional models of Bernardi et al. and Springer et al. provided a framework for many of the multi-dimensional PEMFC models that followed. An isothermal one-dimensional model of the cathode catalyst layer was presented by You and Liu [6]. Current limit conditions at high current densities were predicted by their model. In addition, Burt et al. [7] and Campanari and Iora [8] developed similar multi-dimensional models for solid oxide fuel cells. A two-dimensional model of transport phenomena in PEMFC was presented by Gurau et al. [9]. Wang and Wang [10] presented a three-dimensional dynamic model of a PEMFC to investigate the transient phenomena of electrochemical double layer discharging, gas transport through the gas diffusion layer (GDL) and membrane hydration. Um and Wang [11] elucidated electrochemical kinetics, current distribution, hydrodynamics, and multi-component transport. Maher et al. [12] presented a three-dimensional computational fluid

dynamics (CFDs) model that accounts for species mass transport, heat transfer, potential losses, electrochemical kinetics, and transport of water through the membrane. A two-dimensional CFD model of a PEM fuel cell was developed by Sahraoui et al. by taking into account electrochemical, mass and heat transfer phenomena [13]. Mueller et al. [14] presented a quasi-three-dimensional dynamic model that can capture both the dynamic response characteristics and some effects of cell geometry in a PEMFC model that is simplified enough to be useful in system level simulation and control system development.

In recent years, efforts have been made to investigate the effects of fuel and gas flow geometries on PEMFC performance. Hontanon et al. [15] performed a three-dimensional numerical simulation of the gas flow through the fuel manifold and the fuel side of the bipolar plate, including the anode, for enhancement of PEMFC performance. Parameter sensitivity was analyzed by Junye Wang to determine the influence of geometric structures and parameters on the flow performance of fuel cell stacks [16]. Comparisons of the electrochemical behaviors of direct methanol fuel cells (DMFCs) in serpentine flow fields and in interdigitated flow fields at both the cathode and the anode were conducted by Arico et al. [17]. To better understand the design considerations for bipolar plates, Kumar et al. [18] investigated the effects of the dimensions and shapes of the channels in the flow-field of a bipolar plate by simulating a half-cell. Soler et al. [19] concentrated on studying the effects of backing layer gas permeability and the flow-field pattern on the performance of a PEMFC. The fluid flow and electrochemical reaction in a PEMFC with conventional and interdigitated flow fields was investigated by Hu et al. [20]. They showed that the interdigitated flow field design has better performance, but also has greater pressure loss due to flow through the electrode. Karvonen et al. [21] studied the behavior of reactant and reaction product gas flow in a parallel channel flow field by implementing isothermal two- and three-dimensional PEMFC cathode flow field models. The effects of geometric parameters on PEMFC performance have been examined using CFD calculations by Lee et al. [22]. Ferng et al. [23] investigated the effects of different flow channel designs on the performance of PEMFC using a three-dimensional fuel cell CFD model. The flow channels studied in this work included parallel and serpentine flow types, single-path and multi-path flow channels, and uniform depth and step-wise depth flow channels. CFD simulations were performed by Jeon et al. for four serpentine flow fields with single channel, double channel, cyclic-single channel, and symmetric-single channel patterns to investigate the effects of flow-field design [24]. Jang et al. [25] presented a three-dimensional numerical model of PEMFCs with conventional flow field designs (parallel flow field, Z-type flow field, and serpentine flow field) to investigate performance and transport phenomena in PEMFCs. All of these studies concentrated on the effects of different flow channels, flow channel dimensions and shapes, and flow field designs. In this research, we consider different flow configurations and investigate the effects of inlet flow conditions on each flow configuration systematically.

The objective of this paper is to clarify the interactions between flow configurations and performance in a PEMFC for automotive applications. Additionally, the current research intends to demonstrate the capability of a reduced order (less complex "quasi-three-dimensional") dynamic model to capture the effects of flow configuration while retaining a low computational intensity that is sufficient for use in system simulation and control system development. Using a quasi-three-dimensional approach that simultaneously resolves species, hydration, and temperature makes it possible to identify how the flow configuration and inlet flow conditions affect fuel cell performance. This approach leads to an understanding of how inlet temperature and flow configuration affect the species, hydration, and temperature distributions. From the species, hydration and temperature effects, it is possible to understand how each inlet condition and flow configuration affects cell performance at a fundamental level. In order to investigate the configuration effects of fuel, air, and coolant flows on the performance of PEMFCs, five configurations were used. The effects of humidity and cooling on the performance of the PEMFC were investigated with the type 1 configuration, which has fuel and air counter flow, but a co-flow of air and coolant. A current-power polarization curve is presented to compare the performances of different flow configurations in PEMFCs. Since the model is discretized in quasi-three-dimensions, it is possible to capture the distributions of temperature, current, species mole fractions and membrane water content. In order to validate this model, the simulation results of configuration type 1 were compared with experimental data from a similarly configured PEM unit cell. In order to compare the results with the experiment, one reference point was selected to tune several unknown parameters in the model, and once established, the same parameter values were used for all other conditions.

2. Model description

2.1. PEMFC model

The fuel cell model is based on the work of Mueller et al. [14]. The same electrochemical, water transport and heat transfer equations were used in the fuel cell control volumes as those defined in Mueller et al. However, in the present work, since the experimental fuel cell used has a large active area of 240 cm^2, the previous model was extended by taking the pressure drop of fuel and air as it flows through the gas flow channels into consideration.

2.2. Assumptions

The following is a list of the major assumptions:

1. Control volumes are characterized by a single lumped temperature, pressure, and set of species mole fractions condition.
2. All gases are ideal gases [26].
3. One-dimensional fully developed laminar flow occurs along the stream-wise direction [26].
4. Parallel diffusive fluxes in the gas diffusion layer and membrane are ignored. Convective transport inside the

flow channel dominates parallel diffusive fluxes ($Pe = 10^{10}$) [26].

5. The solid gas diffusion layer (GDL) and membrane electrode assembly (MEA) have a lumped temperature. (The respective Biot number was found to be much less than 0.1.)
6. Each cell in the stack is assumed to operate identically, so that a single cell simulation is taken as being representative and used to calculate full stack performance [8,26].
7. All electrodes are good conductors for which an equipotential electrode surface is assumed [8].
8. Quasi-steady electrochemistry is assumed since the electrochemistry is rapid (occurring at time scales on the order of 10^{-3} s) [27].
9. A single activation polarization equation is used to capture the effects of all physical and chemical processes that polarize the charge transfer process.
10. All reactants generate their ideal number of electrons, and no fuel or oxidant crosses the electrolyte [26].

The fuel cell is discretized into control volumes quasi-three-dimensionally to solve for local states of the fuel cell. The unit cell is discretized in the stream-wise direction, which is shown in Fig. 1. This makes it possible to capture the distributions of current, membrane water content, temperature, and species concentrations. The local resolution not only provides insight into the local performance of the fuel cell, local thermal stresses, local hydrogen and oxygen starvation during transient operation, but can also predict fuel cell dynamic performance more accurately than bulk dynamic models. The unit cell is also discretized in the cross-sectional direction through a unit cell of the fuel cell stack, which is an approach similar to that used by Yuyao and Choe [28] and Freunberger et al. [26]. The primary components of the fuel cell are discretized into seven control volumes, using five types of control volume: (1) solid plate, (2) bulk gas, (3) GDL, (4) membrane electrode assembly (MEA), and (5) coolant, which are shown in Figs. 2 and 3.

Since the gas from the gas channels diffuses through each GDL to the triple phase boundary region of the MEA, resolving the physics, chemistry, and electrochemistry that occur in the perpendicular flow direction (the z-direction in Fig. 1) is

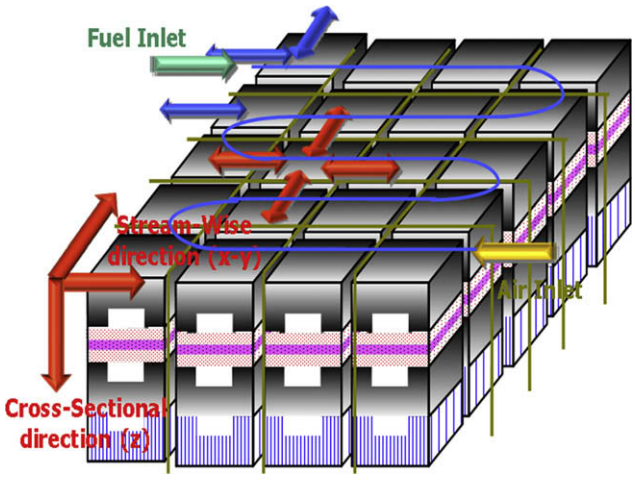

Fig. 1 – Schematic diagram of the PEMFC discretization.

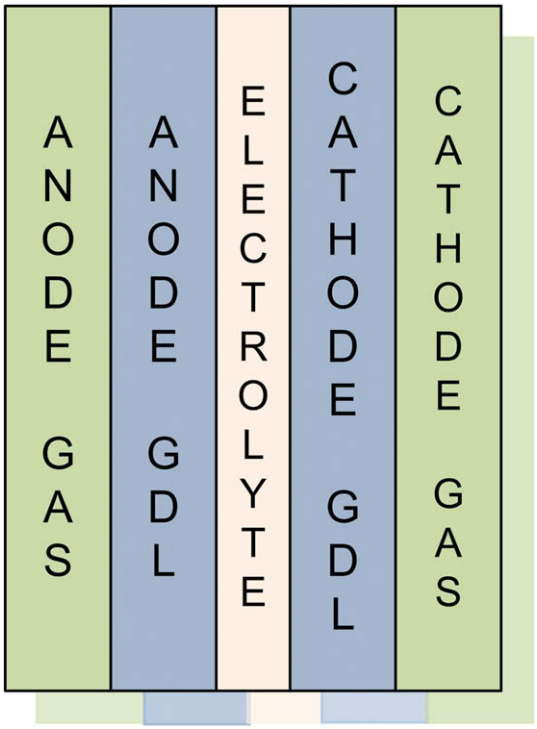

Fig. 2 – Control volumes for species conservation of PEM unit cell (not drawn to scale).

critical to accurately model local species at the triple phase boundary and to capturing membrane hydration, which significantly affects the electrochemical performance of the fuel cell. Significantly large concentration gradients can exist between the bulk gas and the triple phase boundary region. Diffusion fluxes and osmotic water transport to the GDL control volume from electrolyte and gas control volumes are calculated. Without discretization of the perpendicular flow, water transport cannot be accurately resolved. Discretization of the perpendicular flow makes it possible to more accurately model membrane hydration, which is critical to accurately determine overall performance and polarization losses.

While separate GDL and MEA control volumes are essential for resolving the water transport and concentration gradients within the fuel cell, the GDL and MEA can be lumped together into one perpendicular control volume to resolve the perpendicular temperature profile.

Since the dynamic model is for control development and not a model specifically for predicting flooding, two-phase flow and droplet formation in the gas diffusion layer were not considered.

In order to investigate the configuration effects of fuel, air, and coolant flows on the performance of a PEMFC, the model was used to investigate five different flow configuration types. Fig. 4 shows the fuel cell flow configurations, which are labeled type 1 through type 5. The anode and cathode flows of configurations type 1 through type 4 are in counter flow. However, in the case of type 2, the coolant passes directly from the right side to the left side of fuel cell. In the type 3 configuration, the coolant flow is serpentine and perpendicular to the fuel and air flow. In the type 4 configuration, the

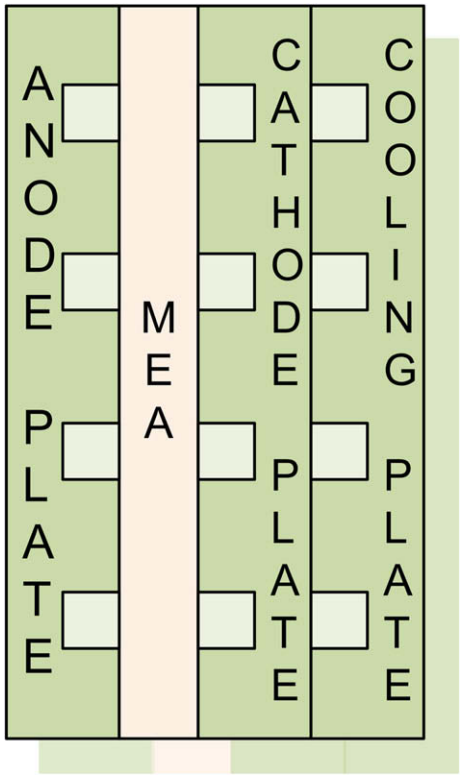

Fig. 3 – Control volumes for energy conservation in the PEM unit cell (not drawn to scale).

coolant channel has the same flow pattern as that of the anode channel. Finally, the type 5 configuration is for a semi-counter-flow cell: the air flows from the right upper side, and turns four times before it flows out the left lower side.

2.3. *Conservation equations*

Temperature, species mole fractions, molar flow rate, and water content of each control volume are solved from conservation first principles. Energy conservation and heat transfer equations are used to solve for temperature, and species conservation and mass transport equations are used to solve for species mole fractions, molar flow rates and water content. The following describes the set of dynamic conservation equations that are solved in each control volume. Subsequent sections describe the flux of species, reactions, and heat transfer between and amongst control volumes as needed to solve each of the conservation equations.

2.3.1. *Energy conservation*

Temperatures throughout the model are determined by solving the dynamic energy conservation equation. Recall that the current model must retain dynamic functionality in order to be useful in system studies and control system development. The temperatures of each solid plate control volumes are found by solving the following ordinary differential equation (ODE):

$$\rho \forall C \frac{dT}{dt} = \sum \dot{Q}_{in} \tag{1}$$

where $\dot{Q}_{in}$ represents heat transfer to the control volume. In a similar fashion, each of the bulk gas and coolant control volume temperatures are determined by solving the dynamic energy conservation equation:

$$NC_V \frac{dT}{dt} = \sum \dot{N}_{in} h_{in} - \sum \dot{N}_{out} h_{out} + \sum \dot{Q}_{in} + \sum \dot{Q}_{latent} \tag{2}$$

where $\dot{N}_{in} h_{in}$ represents the enthalpy flux into the control volume, $\dot{N}_{out} h_{out}$ is the enthalpy flux out of the control volume, $\dot{Q}_{in}$ is the heat transfer to the control volume and $\dot{Q}_{latent}$ represents the latent heat of liquid water evaporating into the bulk gas or vice versa. The temperature of the control volume is taken to be the exit temperature of the control volume, and the inlet temperature of the control volume is that of the node that is upstream (from the ''flow'' perspective) of the exit temperature. Note that the ''upstream'' node can be different for each of the solutions for anode gas, cathode gas, and coolant streams since flows may traverse through the cell differently. This feature must be carefully accounted for in the model. The molar flow rate of each species is determined from species conservation. It is important to mention that the enthalpy flux in the gas control volumes is that of the bulk gas flow, as well as the gas that diffuses to and from the GDL control volume. The enthalpy of the fluid or gas of equation (2) is determined as:

$$h = \sum \vec{X} \left(\int_{T=298K}^{T} C_P dT \right) \tag{3}$$

where $\vec{X}$ are the component mass fractions and C_P are the temperature dependent specific heats at constant pressure for each species. The number of moles in the control volume of equation (2) can be determined from the ideal gas law:

$$N = \frac{P\forall}{RT} \tag{4}$$

The temperature of each lumped GDL and MEA control volume is found by combining the gas and solid control volume conservation equations. In addition, irreversibilities associated with the electrochemical reactions are modeled as heat generated in this control volume as follows.

$$\left(\sum (\rho \forall C)_s + \sum (NC)_l \right) \frac{dT}{dt} = \dot{N}_{in} h_{in} - \dot{N}_{out} h_{out} + \sum \dot{Q}_{in} + \sum \dot{Q}_{latent} + \Delta H \cdot \frac{I}{nF} - \frac{V \cdot I}{1000} \tag{5}$$

where ΔH is the enthalpy of formation of water, I is the fuel cell current, and V is the fuel cell voltage. From each conservation of energy ODE, it is possible to directly determine the temperature of each control volume, which is assumed to be the same as the control volume exit temperature.

2.3.2. *Species conservation*

As energy conservation is used to determine the temperature of each control volume, the species mole numbers at each gas control volume exit is determined from species mass conservation. Specifically, the exit mole number of each bulk gas control volume is found from the following species conservation equation:

$$\frac{d(N\vec{X})}{dt} = \dot{N}_{in} \vec{X}_{in} - \dot{N}_{out} \vec{X}_{out} + \sum \vec{\Phi} \tag{6}$$

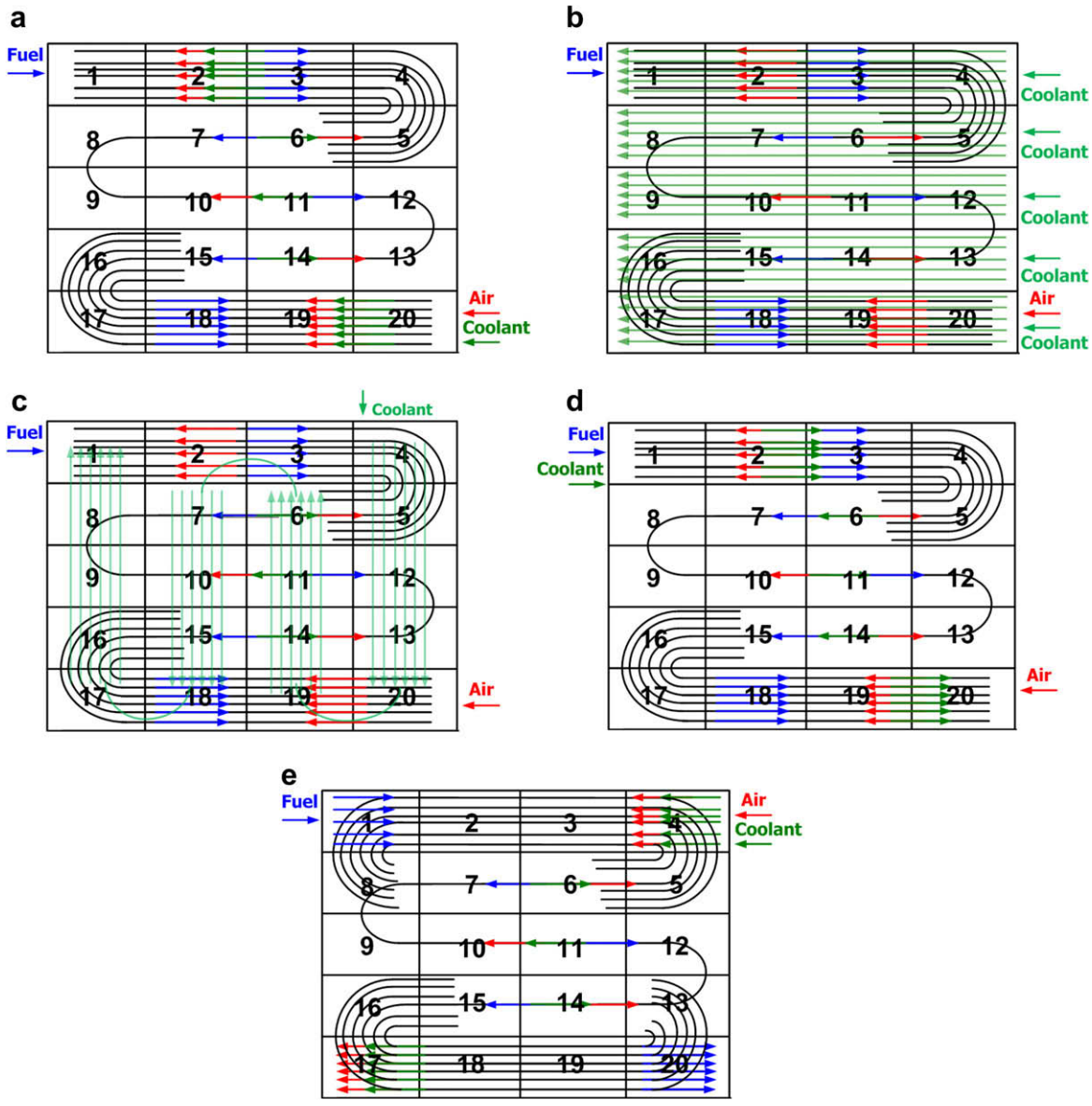

Fig. 4 – Schematic diagram of type 1 (a) through type 5 (e) cell configurations.

The exit molar flow rate is determined from the total species conservation equation:

$$\dot{N}_{out} = \dot{N}_{in} + \sum \vec{\Phi} - \sum \frac{d(N\vec{X})}{dt} \quad (7)$$

In Eqs. (6) and (7), $\vec{\Phi}$ is the species diffusion flux from adjacent GDL control volume. In order to solve for the exit mole fraction, and molar flow rate, the control volume mole fractions are assumed to be those of the control volume exit condition. We apply this "perfectly stirred" assumption to all gas and liquid control volumes in the model.

Local electrochemical reactions rates for each species ($\dot{\vec{R}}$) are modeled in the GDL control volume. The species mole number of each GDL control volume is determined as follows.

$$\frac{d\vec{N}}{dt} = -\sum \vec{\Phi} + \sum \Psi_{H_2O} + \sum \Theta_{H_2O} + \dot{\vec{R}} \quad (8)$$

where Ψ_{H_2O} is the water diffusion flux from the adjacent MEA control volume, and Θ_{H_2O} is the amount of water osmotic flux through the MEA (between the two GDL control volumes) within each node. From species mole numbers, the species mole fraction and concentrations within GDL control volumes can readily be determined:

$$\vec{X} = \frac{\vec{N}}{\sum \vec{N}} \quad (9)$$

$$\vec{C} = \frac{\vec{N}}{V} \quad (10)$$

Species conservation is further used to calculate the amount of water in the local MEA control volumes as follows:

$$\frac{dN_{H_2O}}{dt} = -\sum \Psi_{H_2O} \quad (11)$$

from local water content (λ) can be determined by:

$$\lambda = \frac{N_{H_2O}}{\forall_m} \cdot \frac{M_m}{\rho_m} \tag{12}$$

where $\forall_m$ is the membrane dry volume, M_m is the membrane dry equivalent weight, and ρ_m is the membrane dry density. This local membrane water content, which significantly impacts membrane ionic conductivity, must be resolved to accurately determine fuel cell performance.

From the species mass conservation ordinary differential equations, it is possible to determine the species mole number in each of the bulk gas streams, each GDL, and in the MEA control volume of a single node. In addition, with the perfectly stirred assumption, these ODEs define exit molar flow rates in bulk gas control volumes. The species mole number can then be used to determine mole fractions, concentrations, and membrane water content as appropriate. In general, the current approach and set of assumptions allows dynamic equations that can account for all species in each major subcomponent of the fuel cell repeat unit to be solved. In the present model, four species are considered: hydrogen, oxygen, nitrogen and water, since the modeled fuel cell operates on pure hydrogen and air.

2.4. Heat transfer

As described, energy conservation equations are used to determine temperatures throughout the fuel cell. Specifically Equation (1) is used to determine solid plate temperatures, Equation (2) is used to determine bulk gas and coolant temperatures, and Equation (5) is used to determine the temperatures of MEA and GDL control volumes. In each of the three equations, the extent of heat transfer between adjacent control volumes needs to be defined.

Heat is generated in the fuel cell due to irreversibilities in the electrochemical reactions. Recall that the impact of these irreversibilities on energy conservation is accounted for in the solution of the bulk GDL and MEA thermal control volume as the difference between the total energy available from the global electrochemical reaction,

$$H_2 + \frac{1}{2}O_2 \rightarrow H_2O \tag{13}$$

and the amount of energy exiting the fuel cell as electricity ($\Delta H \cdot I/nF - V \cdot I/1000$). In the perpendicular direction, the heat generated in the GDL and MEA layer, is transferred in part to the bulk gas through convection heat transfer and by diffusion of species from the GDL to the bulk gas. In addition, some heat from the electrolyte and GDL is transferred to the solid plate through conduction. The heat in the solid plate is then transferred to the coolant channel, through convection. The electrode (solid plate) is in thermal contact with the GDL, coolant channel, as well as the bulk gas. As a result, heat can transfer between the bulk gas and the solid plate electrode. Note, in addition, that heat is transferred between and amongst adjacent nodes. The amount of heat generated at each location in the fuel cell can vary depending on the amount of current generated locally in the fuel cell. This variation, combined with the effects of flow-oriented convective heat transfer and variations in gas and coolant flow rates and properties can lead to significant temperature gradients in the MEA and solid plates of the fuel cell. These gradients are somewhat ''smoothed'' by in-plane conduction heat transfer. Thus, in addition to capturing heat transfer in the perpendicular, conduction heat transfer between adjacent solid plates and natural convection at the edge of each plate is captured in the flow plane. Conduction heat transfer is not modeled in the MEA because this layer is very thin.

Throughout the model, convection heat transfer between solid and gas nodes are determined from Newton's law of cooling:

$$\dot{Q} = A \cdot h \cdot (T_2 - T_1) \tag{14}$$

The convection coefficient (h) is determined from the Nusselt number (Nu_D) provided by Incropera and Dewitt [29]:

$$h = \frac{Nu_D \cdot k_f}{D_H} \tag{15}$$

where k_f is the fluid conduction heat transfer coefficient, and D_H is the hydraulic diameter.

Conduction heat transfer throughout the model is determined from Fourier's law:

$$\dot{Q} = \frac{A \cdot k_s \cdot (T_2 - T_1)}{L} \tag{16}$$

2.5. Species diffusion, osmotic drag and reactions

Species diffusion ($\vec{\Phi}$, Ψ_{H_2O}), osmotic drag (Θ_{H_2O}), and reaction rates ($\vec{R}$) in the fuel cell, presented in the mass conservation equations, are resolved in the model. The electrochemical reactions are modeled in the GDL control volumes, which represent the regions of triple phase boundaries in the current fuel cell model. The anode half reaction is:

$$H_2 \rightarrow 2H^+ + 2e^- \tag{17}$$

and the cathode half reaction is:

$$\frac{1}{2}O_2 + 2H^+ + 2e^- \rightarrow H_2O \tag{18}$$

with a global reaction as shown in Equation (13). From Faraday's law, the reaction rate of both half reactions is directly proportional to the current as follows:

$$\dot{R}_{H_2O} = -\dot{R}_{H_2} = -2\dot{R}_{o_2} = \frac{I}{n \cdot F} \tag{19}$$

Species diffusion is captured in the perpendicular direction between gas, GDL, and MEA control volumes. Species transport from the gas channel to the GDL accounts for the convection driven by a concentration gradient and diffusion in the GDL. The mass transport coefficient ($\vec{g}_m$) at the gas channel and GDL interface is obtained based on the Reynolds analogy between heat and mass transfer:

$$\vec{g}_m = \frac{Sh \cdot \vec{D}_m}{D_H} \tag{20}$$

where Sh is the Sherwood number, $\vec{D}_m$ is the diffusion coefficient, and D_H is the hydraulic diameter of the gas flow channel. The diffusion coefficients for species are functions of temperature and pressure and are modified via the

Bruggeman correlation to account for the effects of porosity and tortuosity in the GDL as follows:

$$\vec{D}_m = \vec{D}_o \left(\frac{T}{T_o}\right)^{3/2} \left(\frac{P_o}{P}\right)$$

$$\vec{D}_m^{\,\text{eff}} = \varepsilon^{1.5} \cdot \vec{D}_m \tag{21}$$

where $\vec{D}_o$ is the species diffusion coefficient at standard pressure and temperature, $\vec{D}_m^{\,\text{eff}}$ is the effective species diffusion coefficient and ε is the GDL porosity. The species diffusion flux between the GDL and bulk gasses is then:

$$\vec{R}_{\text{dif}} = A \cdot \frac{1}{\frac{1}{\vec{g}_m} + \frac{t_{\text{gdl}}}{\vec{D}_m^{\,\text{eff}}}} \tag{22}$$

$$\vec{\Phi} = \vec{R}_{\text{dif}} \cdot (\vec{C}_2 - \vec{C}_1) \tag{23}$$

where $\vec{R}_{\text{dif}}$ is the total diffusion resistance of each species and t_{gdl} is the thickness of the GDL.

2.5.1. *Water transport*

Since water content in the membrane strongly affects ionic conductivity, the current dynamic model captures the details of water behavior in the MEA. Two types of water molecule transport from the anode or cathode GDL to the MEA are considered: (1) the electro-osmotic drag, and (2) diffusion due to a concentration gradient between control volumes.

The rate of water molecule transport via osmotic drag from the anode-electrolyte interface to the cathode-electrolyte interface is proportional to current density and the electro-osmotic drag coefficient as follows:

$$\Theta_{H_2O} = n_d \cdot \frac{I}{A \cdot F} \tag{24}$$

The osmotic drag coefficient (n_d), is calculated from the membrane water content (λ), which depends on the water activity (a) [30]:

$$n_d = 0.0029\lambda^2 + 0.05\lambda - 3.4 \times 10^{-19} \tag{25}$$

$$\lambda = \begin{cases} 0.043 + 17.81a - 39.85a^2 + 36a^3 & \text{for } 0 < a \le 1 \\ 14 + 1.4(a-1) & \text{for } 1 < a \le 3 \end{cases}$$

The water diffusion due to the concentration gradient between the two GDL and MEA control volumes is calculated by:

$$\Psi_{H_2O} = D_w \cdot A \cdot \frac{(C_2 - C_1)}{t_{\text{mea}}} \tag{26}$$

where D_w is the diffusion coefficient of water in the electrolyte and t_{mea} is the thickness of the MEA. The water concentration in the membrane is calculated from the membrane water content:

$$C = \frac{\rho_m}{M_m} \cdot \lambda \tag{27}$$

where ρ_{mem} is the membrane dry density and M_{mem} is the membrane dry equivalent weight. The diffusion coefficient of water in the electrolyte (D_w) is calculated from the empirical Equation [30]:

$$D_w = D_\lambda \cdot \exp\left[2416\left(\frac{1}{303} - \frac{1}{T}\right)\right] \tag{28}$$

where

$$D_\lambda = \begin{cases} 10^{-6} & \text{for } \lambda < 2 \\ [1 + 2(\lambda - 2)] \times 10^{-6} & \text{for } 2 \le \lambda \le 3 \\ [3 - 1.67(\lambda - 3)] \times 10^{-6} & \text{for } 3 < \lambda < 4.5 \\ 1.25 \times 10^{-6} & \text{for } 4.5 \le \lambda \end{cases}$$

2.6. *Electrochemical model*

It is possible to determine the fuel cell operating voltage, and current generation distribution throughout the fuel cell by resolving species mole fractions, molar flow rates, and temperatures dynamically throughout the fuel cell and by assuming the fuel cell voltage is in quasi-equilibrium with the dynamic state of the fuel cell (Assumption 9). It is important to note that, since the fuel cell electrodes are good electron conductors, the voltage difference across any one cell is assumed to be constant for all parts of the cell (equipotential Assumption 8). As a result each nodal current must be determined such that all node voltages differences are equivalent. Before explaining the solution procedure, the voltage–current relationships are explained.

Each nodal voltage is determined by subtracting the locally calculated activation and ohmic polarization from the Nernst voltage:

$$V_{\text{node}} = V_{\text{Nernst}} - V_{\text{act}} - V_{\text{ohm}} \tag{29}$$

The Nernst voltage at each node is determined based upon the MEA temperature, and the local species mole fractions in the GDL control volumes, which are assumed to represent the concentrations at the triple phase boundary.

$$V_{\text{Nernst}} = \left(-\frac{\Delta G(T)}{n \cdot F} + \frac{R \cdot T}{n \cdot F} \ln\left[\frac{X_{H_2} \cdot X_{O_2}^{1/2}}{X_{H_2O}} \cdot p^{1/2}\right]\right)_{\text{GDL}} \tag{30}$$

The activation polarization is modeled from the Tafel equation based on the local GDL control volume states:

$$V_{\text{act}} = \left(a_c \frac{R \cdot T}{n \cdot F} \ln\left(\frac{I/A}{i_o}\right)\right)_{\text{GDL}} \tag{31}$$

The ohmic polarization is modeled as determined for Nafion 117 [4] based upon the electrolyte control volume temperature and hydration as follows:

$$V_{\text{ohm}} = \left(I \frac{t_m}{b_1 \exp\left(b_2\left(\frac{1}{303} - \frac{1}{T}\right)\right)}\right)_{\text{MEA}} \tag{32}$$

$$b_1 = 0.005139\lambda - 0.00326 \tag{33}$$

$$\sigma(T, \lambda) = b_1 \exp\left(b_2\left(\frac{1}{303} - \frac{1}{T}\right)\right) \tag{34}$$

The voltage is determined at each node from Equations (14)–(19), but to satisfy the equipotential assumption, each nodal voltage must be equivalent. In addition, the fuel cell must satisfy Ohm's law for the external circuit.

$$V_{\text{node}} = V_{\text{cell}} = \sum I_{\text{node}} \cdot R \tag{35}$$

That is, the sum of all the nodal currents multiplied by the external resistance must be equal to each nodal voltage, or to the cell voltage. As a result, each nodal current is iterated until all the nodal voltages are equivalent and Ohm's law is satisfied. It is important to note that the amount of current produced at each node affects species mole fractions, and temperatures throughout the fuel cell.

2.6.1. Pressure drop

In order to determine the accurate Nernst voltage of each local section of the fuel cell, the local anode and cathode channel pressures should be precisely calculated. Furthermore, in this study, the pressure loss of the coolant flow due to bends and turns and flow in coolant channels was used to predict the required coolant pump power. Since the model is for a unit cell, only the pressure loss caused by the cell was considered. In other words, the pressure loss in the stack manifold due to distributing the fuel and air to each unit cell, pressure drops in external plumbing and other components of the thermal management system, such as a radiator, were not simulated. In order to determine the friction factor of each flow, the Reynolds number is calculated. Flow that has a Reynolds number under 2100 was assumed to be laminar flow, whereas flow with a Reynolds number above 2100 was considered to be turbulent flow. The Reynolds number, friction factor, head loss due to length and bends, and wasted pump power were determined based on the following expressions [31]:

$$\mathrm{Re} = \frac{\rho v D_{\mathrm{H}}}{\mu} \tag{36}$$

$$\mathrm{Re} \le 2100 \quad f = \frac{64}{Re} \tag{37}$$

$$3000 \le Re_D \le 5 \times 10^6 \quad f = (0.79\ \ln Re_D - 1.64)^{-2} \tag{38}$$

$$h_m = f\frac{L}{D_H}\frac{v^2}{2g} = K\frac{v^2}{2g} \tag{39}$$

$$P_{\mathrm{pump}} = \frac{\Delta p_{\mathrm{drop}}\dot{m}}{\eta_v \eta_m \eta_h \rho} = \frac{\Delta p_{\mathrm{drop}}\dot{m}}{\eta\rho} \tag{40}$$

K is a dimensionless loss coefficient, which is shown in Table 1. η_v, η_m, and η_h are volumetric, mechanical, and hydraulic efficiency, respectively, which were assumed to be 1 in this study [31].

2.6.2. Interaction of temperature, humidity and membrane hydration

The local electric resistance of the MEA is directly determined by membrane water content, which was determined from inlet water conditions and concurrent solution of equations that govern water production on the cathode side and osmotic drag and diffusion flux of water flow through the membrane. Membrane hydration is also highly dependent upon the temperature of the membrane and humidity conditions of anode and cathode. The effects of these two factors on the membrane water content depend upon the operating conditions, such as inlet relative humidity, temperature, and local current density. If the membrane is not well hydrated, the electrical resistance is increased, such that areas of low membrane hydration will exhibit increased ohmic losses that lower the fuel cell performance. Local electrical resistance and overpotentials vary with local temperature and water content, but the potential difference on the PEMFC is constant across the cell. However, local current density is affected by the local temperature and water content fields that satisfy the electrochemical model equations while maintaining a single cell voltage.

If the active area of a fuel cell is small, the temperature distribution of the fuel cell can be neglected. However, PEMFC with large active areas for high power output applications typically have significant temperature gradients that must be taken into accounted. The temperature of the coolant inlet was set at 338 K, and the coolant outlet temperature was maintained at 343 K by adjusting the coolant flow rate. To avoid vapor condensation in the channel, the gas temperatures were set to the same value as the coolant inlet temperature. As expected, the fuel cell temperature was at its maximum around the coolant channel exit and at its minimum around the coolant channel entrance. The gas temperature was highly dependent upon the fuel cell temperature because the gases have small thermal capacity. Gases were typically heated up immediately after entering the channel inlet by heat transfer from the fuel cell. Then, depending upon the coolant flow configuration, the gas temperatures tended to either slowly decrease or increase along the channel. As the gas was heated, the relative humidity of the gas and the water activity in the cathode GDL dramatically decreased, which ultimately led to local membrane drying in some cases. The water production at the cathode side gradually increased in the direction of flow along the channel. However, when the temperature of the membrane electrolyte was relatively high with comparatively low cathode inlet humidity, the amount of water formed near the cathode inlet was not sufficient to saturate the cathode GDL. This eventually decreased the net water flux through the membrane and resulted in reduced membrane hydration.

The degree of membrane hydration is determined by the net water flux through the membrane between the anode GDL and cathode GDL. Since the water concentration of the cathode GDL is relatively higher than that of the anode GDL, because water is formed in the cathode GDL, the water concentration of the cathode GDL becomes the critical factor that determines the membrane water content.

2.6.3. Experimental setup

In order to verify the simulation results, a unit cell of a PEMFC with an active area of 240 cm^2 was used in this work. The width and height of a unit cell are 200 mm and 118 mm, respectively. The single cell contained 6 serpentine flow paths

Table 1 – Resistance coefficients for elbows.

	Nominal diameter, in (Flanged)		
	1	2	4
90° Regular	0.50	0.39	0.30
90° Long radius	0.40	0.30	0.19
180° Regular	0.41	0.35	0.30
180° Long radius	0.40	0.30	0.21

Table 2 – Model parameter values.

Description geometry	Value
Cell width (x)	0.2 m
Cell height (y)	0.118 m
Depth of anode gas channel (z)	0.001 m
Depth of cathode gas channel (z)	0.001 m
Depth of cooling channel (z)	0.001 m
Thickness of GDL (z)	0.0002 m
Thickness of electrolyte (z)	30.48×10^{-6} m
Thickness of separator plates (z)	0.002 m
GDL porosity	0.5

in the anode, cathode and coolant. The depth and width of the anode and cathode flow channels are 1 mm and 2 mm, respectively. The 6 channel flow turns 4 times. The anode and cathode flows are in a counter-flow configuration. The coolant flow has the same configuration as the cathode flow. The flow patterns in the experimental cell correspond to those of type 1. The MEA used in this work is based on Nafion®, and its thickness is 30.48 μm. The temperature of the fuel cell was controlled by the coolant water inlet temperature and flow. The specifications of the PEMFC are presented in Table 2.

The fuel cell is operated in a PEMFC test station. A schematic diagram of the test station for the 240 cm^2 fuel cell is shown in Fig. 5. High purity hydrogen (99.999%) at the anode and high purity air are used as reactant gases, and they are humidified by passing through a membrane humidifier. High purity nitrogen is supplied for purging between experimental cases. The coolant temperature is controlled by a PID temperature controller (Yokogawa Inc.). The humidity of the anode and cathode is controlled by the membrane humidifier, whose performance was verified and monitored by a humidity sensor. The cell current is controlled by an electric load (AMREL Inc.). Data acquisition is accomplished using a USB 6009 (National Instrument) board and a custom LabVIEW® program to rapidly obtain accurate performance data. The cell voltage data are obtained at 100 Hz.

3. Results and discussion

3.1. Model comparison to experimental data

The quasi-three-dimensional dynamic PEMFC model was used in this study to simulate the measured polarization curve of a unit PEMFC. Since the model does not include the two-phase flow effect and droplet formation in the gas diffusion layer, the experiment was performed at the condition that no liquid water droplets appeared to be present in the cathode compartment. A single point presented in Table 3 was selected to tune several unknown parameters in the model, namely, the constants used in the polarization expressions. In order to tune the ohmic loss and activation loss in the model, b_2 in Equation 34 and a_c in Equation 31 were changed, respectively, and are represented in Table 4. Once these polarization constants are established, they are held constant for all other simulations. Fig. 6 presents the comparison between polarization curves from the simulation and the experiment. The fuel flow rate and air flow rate were set to 1.01 and 3.00 LPM, respectively, for this comparison. The operating temperature and pressure were 65 °C and 110 kPa, respectively. The simulation result is in good agreement with the experimental data.

3.2. Comparison of performance amongst the five flow configuration types

To compare the performance of the five different flow configurations, polarization curves are produced over the range of current density from 0.1 A/cm^2 to 1 A/cm^2 as presented in Fig. 7. The generated net powers of the five

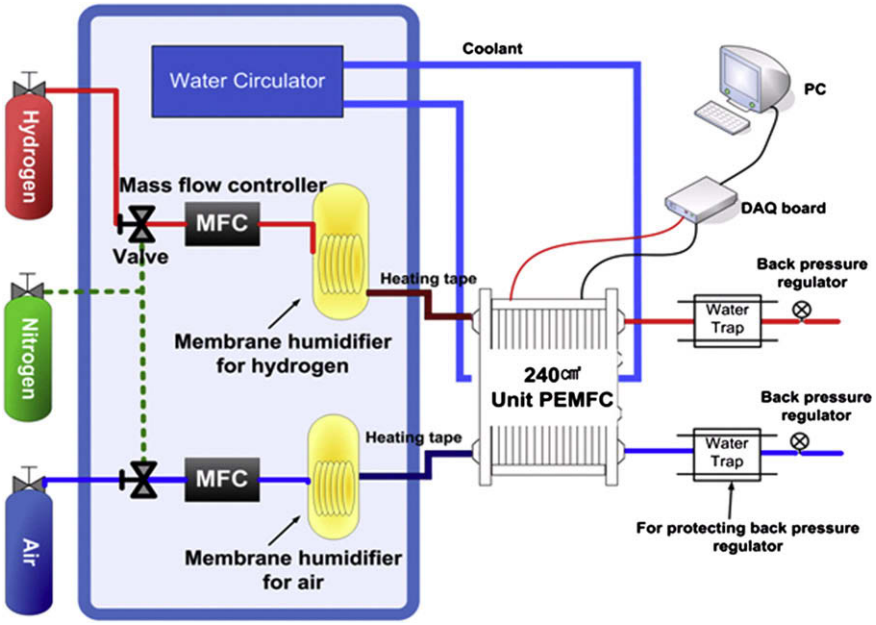

Fig. 5 – Schematic diagram of the experimental setup.

Table 3 – Operating conditions of the reference point.

Humidity	60%	Temperature	65 °C
H_2 flow rate	1.01 lpm	O_2 flow rate	3 lpm
H_2 Utility	0.52	O_2 Utility	0.33
Current	0.744 A/cm^2	Pressure	110 kPa

configuration types are very similar in the low current density region under approximately 0.13 A/cm^2. However, as the current density becomes higher than 0.13 A/cm^2, the power produced by each configuration is different. The type 1 configuration has the highest power and voltage when the current density is above 0.13 A/cm^2. The power produced by type 2 and type 3 configurations is almost the same, and it is only slightly different up to a current density of 0.74 A/cm^2. At higher current densities, the power of the type 2 configuration sharply decreases and finally becomes the lowest at nearly 1 A/cm^2. In the case of the type 4 and type 5 configurations, they have the same, lowest power up to a current density of 0.40 A/cm^2. However, the power produced by the type 5 configuration sharply increases above a current density of 0.74 A/cm^2 and becomes the highest around 1 A/cm^2. The power of the type 4 configuration is a little bit higher in the current density range from 0.40 to 0.74 A/cm^2, then becomes lower than that of type 5 at a current density of 1 A/cm^2.

3.3. *Configuration effects*

In order to clarify the interactions between the performance of the cell and the configuration of fuel, air, and coolant flows, the distribution of current density, membrane water content, and temperature of all configurations at a current density of 0.74 A/cm^2 and 1 A/cm^2 were compared. Fig. 8 shows a comparison of water content and temperature in the membrane for all configurations at a current density of 0.74 A/cm^2. In the type 1 configuration, since the coolant flow is concurrent with that of the cathode flow, the temperature of the membrane decreases in the direction of anode channel flow. Even though the saturation pressure of the cathode GDL decreased in this direction, it became higher than the water vapor pressure beyond the 17th nodal section due to low cathode inlet humidity. As a result, the lowest membrane water content occurs at the cathode inlet. While the coolant flow configurations of type 2 and type 3 cells are different, the temperature distributions of these two configurations are almost the same. As a result, they have a similar distribution of membrane water content. In these two configurations, there are temperature oscillations along the anode channel resulting from the cross-flow coolant configuration. Since the temperatures near the cathode inlet in these two models are relatively higher than that of the type 1 configuration,

Table 4 – Tuning parameters for validation.

a_c	b_2
1.95	350

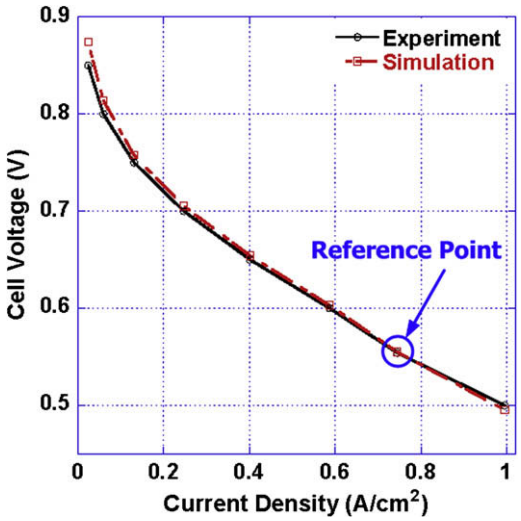

Fig. 6 – Comparison between experimental and simulated polarization curves.

membrane hydration begins to drop earlier than for a type 1 configuration (beyond the 15th nodal section). This means that at the 15th nodal section, when the temperature of the membrane electrolyte is higher than that of the type 1 configuration, the cathode GDL cannot be saturated. Since the coolant flow of the type 4 configuration is concurrent with the fuel flow, the temperature of the cell increases along the anode flow direction. This means that saturation pressure in the cathode GDL gradually increases in the direction of anode flow and can be increased to levels that are higher than water vapor pressure in that local section. As a result, the membrane water content in type 4 cells starts to fall from the 13th nodal section. This indicates that when the temperature of the membrane is higher than that of the type 1 configuration, at the 13th nodal section, the saturation pressure is higher than

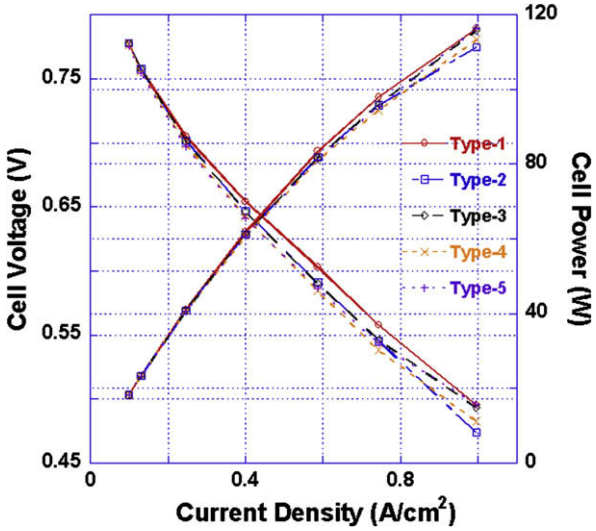

Fig. 7 – Comparisons of voltage and power vs. current density for type 1 through type 5 configurations of the PEMFC.

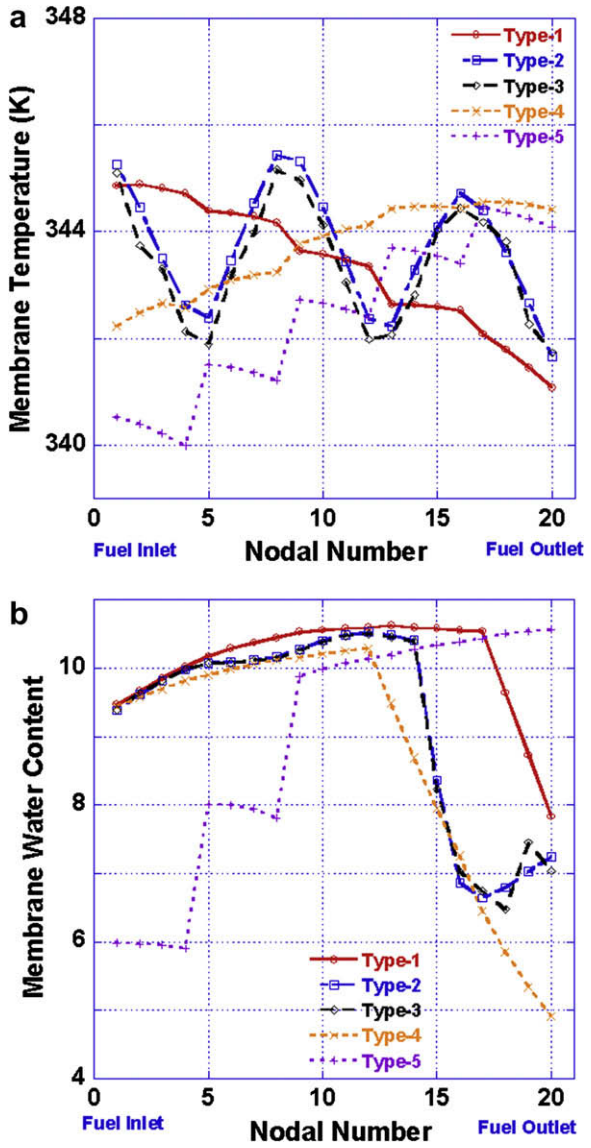

Fig. 8 – Comparisons of membrane water content and membrane temperature along the anode channel for type 1 through type 5 configurations for the PEMFC at a cell current density of 0.74 A/cm^2.

water vapor pressure in cathode GDL. In the case of the type 5 configuration, the coolant and air inlet is at the 4th nodal section with flow that is counter to the anode flow in the same row, and with flow that exits at the 17th nodal section. Since the cathode inlet is close to the fuel inlet, the amount of water formation and the partial pressure of water vapor in the local sections near the inlet are very low compared to that of other configurations; low inlet humidity of anode and cathode gases results in low membrane water content in this section. However, since both the fuel and air flow in nearly the same direction, the amount of water formation and the partial pressure of water vapor are increased in the direction of fuel flow. Since the increasing rate of water vapor pressure due to these two effects is higher than that of water saturation pressure due to increasing temperature, eventually the membrane hydration increases in the fuel flow direction. That is, the temperature ends up not being the determining factor for membrane hydration in the type 5 configuration.

Comparisons of membrane water content and temperature for types 1–5 configurations at a cell current density of 1 A/cm^2 are shown in Fig. 9. When the operating current density is increased, the amount of water formation is increased as well. In other words, the temperature effect on the membrane hydration in the area of low membrane water content at the current density of 1 A/cm^2 is reduced compared to that occurring at a current density of 0.74 A/cm^2. The membrane in the type 1 and type 5 configurations is nearly uniformly hydrated over the whole cell area. Further, in the type 3 configuration, the membrane water content suddenly

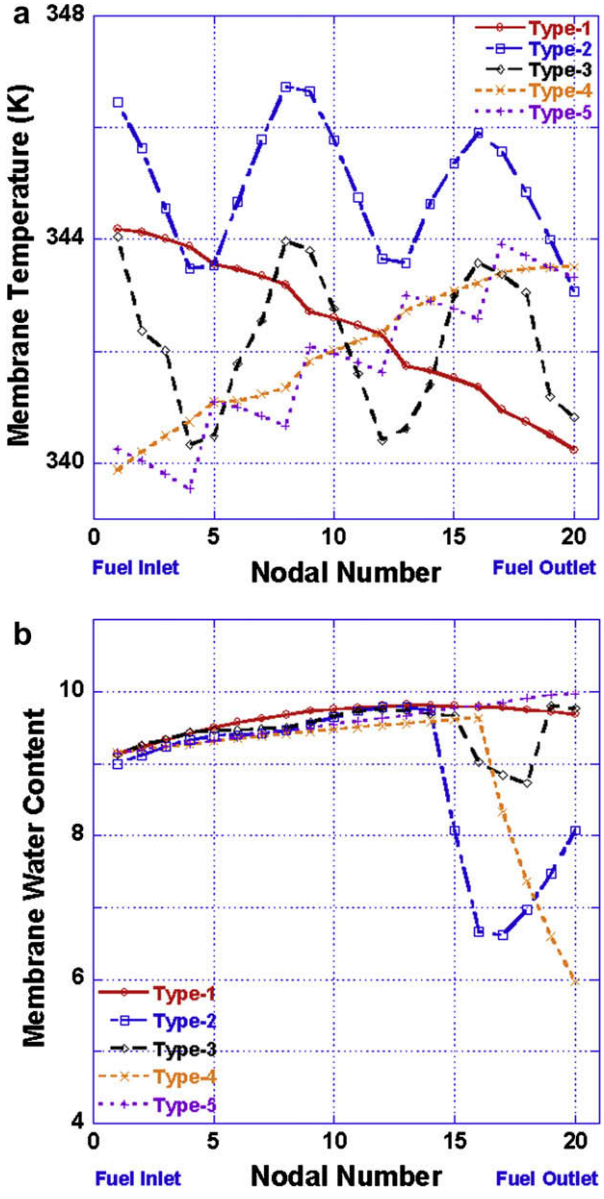

Fig. 9 – Comparisons of membrane water content and membrane temperature along the anode channel for type 1 through type 5 configurations for the PEMFC at cell current density of 1 A/cm^2.

decreases from the 16th local section to the 18th local section and recovers its value beyond the 19th local section. Furthermore, the membrane water content in the type 4 configuration decreases from the 16th local section on. This shows that the membrane is more hydrated compared to that in a cell operated at a current density of 0.74 A/cm^2. In addition, the type 2 configuration has almost the same behavior at cell current densities of 0.74 A/cm^2 and 1 A/cm^2, but the membrane near the cathode inlet is more hydrated at higher current density due to greater water formation.

The power needed to operate a vehicle is the net system power determined by subtracting the parasitic power of auxiliary systems from the power generated by the fuel cell stack. In this study, to investigate an element of parasitic loss, the power of the coolant pump associated with different flow configurations was estimated by calculating the pressure loss of coolant flow. Tables 5 and 6 illustrate the comparison of voltage, pump power, and net power among the five flow configurations at a current density of 0.74 A/cm^2 and 1 A/cm^2, respectively. For operation at a current density of 0.74 A/cm^2, the membrane of the type 1 configuration is well hydrated over the whole cell area and the area that exhibits low membrane water content is smallest, so that type 1 has the highest performance even though the coolant pump power is relatively large compared to that of type 2 and type 3. The coolant pump power of the type 3 configuration has a ten times higher value than that of type 2. The power generated by the type 3 configuration is also higher than that produced by type 2. Thus, the net power of type 2 and type 3 configurations are similar with slight differences. The type 4 configuration has the lowest membrane hydration while the highest coolant pump power, which leads to the lowest cell voltage and the lowest net power for an operating current density of 0.74 A/cm^2. When the cell current density is 1 A/cm^2, the type 5 configuration has the most hydrated membrane, leading to the highest performance. Moreover, the type 2 configuration has the lowest performance due to its large area of low membrane hydration. As the operating current density is increased, the relative pump loss values among the configurations are changed. However, the net power scales directly with generated power. Generally, since the parasitic pump power is small compared to the generated power, the pump loss does not have a large effect on the net performance of the PEMFC.

In this study, the effect of gas humidity and temperature on the performance of the fuel cell was also investigated with the type 1 configuration. The type 1 configuration was operated with various temperature differences between coolant inlet and outlet, 2 K, 3.2 K, 3.3 K, and 4 K. The type 1 configuration was also examined for a variety of inlet anode and cathode relative humidity values, for instance 70–70% and 80–80%. The voltage and power of the type 1 configuration for various temperature differences between coolant inlet and outlet are shown in Table 7. Fig. 10 shows a comparison of the temperature and water content of the membrane for these conditions. As the temperature difference between coolant inlet and outlet decreased, the temperature at the cathode inlet also decreased. When the temperature difference rose to 3.2 K, the temperature at the cathode inlet became approximately 339 K. Moreover, the cathode GDL at all sections began to be saturated over the whole cell area. At the temperature difference of 3.3 K, only a portion of cathode inlet is not saturated. As the temperature difference is increased to 4 K, the distribution of membrane water content along the anode channel was almost the same as that of a temperature difference of 5 K. In order to elucidate the fundamental reasons for this coolant temperature effect on the performance of PEMFC, we temporarily focus upon the 20th nodal section of the model at the cathode inlet with low inlet humidity of 60% (for both anode and cathode) and a coolant temperature difference between inlet and outlet of 4 K and 5 K. Characteristics of PEMFC, such as water flux, are compared in Table 8. When the temperature difference between coolant inlet and outlet is 4 K and 5 K, the temperature of the membrane at the 20th local section is 340.9 K and 341.1 K, respectively. As the temperature of the membrane is increased from 340.9 K to 341.1 K, the total diffusion resistance between channel and GDL decreases. This means that as temperature is increased, the amount of water flux toward the anode GDL from the anode channel and toward the cathode channel from the cathode GDL are increased. Even

Table 5 – Comparison of voltage, power and pressure loss from type 1 to type 5 fuel cell model at cell current density of 0.74 A/cm^2.

	Type 1	Type 2	Type 3	Type 4	Type 5
Mean membrane water content	10.08	9.24	9.23	8.77	8.94
Voltage (V)	0.558	0.545	0.546	0.538	0.543
Generated power (W)	97.95	95.78	95.92	94.5	95.44
Pump power (W)	0.025	0.001	0.013	0.029	0.026
Net power (W)	97.93	95.78	95.91	94.47	95.41

Table 6 – Comparison of voltage, power and pressure loss from type 1 to type 5 fuel cell model at cell current density of 1 A/cm^2.

	Type 1	Type 2	Type 3	Type 4	Type 5
Mean membrane water content	9.63	8.82	9.45	8.94	9.56
Voltage (V)	0.495	0.474	0.493	0.483	0.496
Generated power (W)	116.36	111.30	115.84	113.49	116.52
Pump power (W)	0.105	0.002	0.009	0.009	0.008
Net power (W)	116.26	111.30	115.83	113.48	116.51

Table 7 – Comparison of voltage, power and pressure loss of type 1 model at the cell current density of 0.74 A/cm^2 with various temperature differences between the coolant inlet and outlet.

Temperature difference	2	3.2	3.3	4	5
Voltage (V)	0.570	0.567	0.567	0.559	0.558
Generated power (W)	100	99.6	99.54	98.2	97.95
Pump power (W)	0.425	0.144	0.135	0.039	0.024
Net power (W)	99.58	99.46	99.41	98.16	97.93

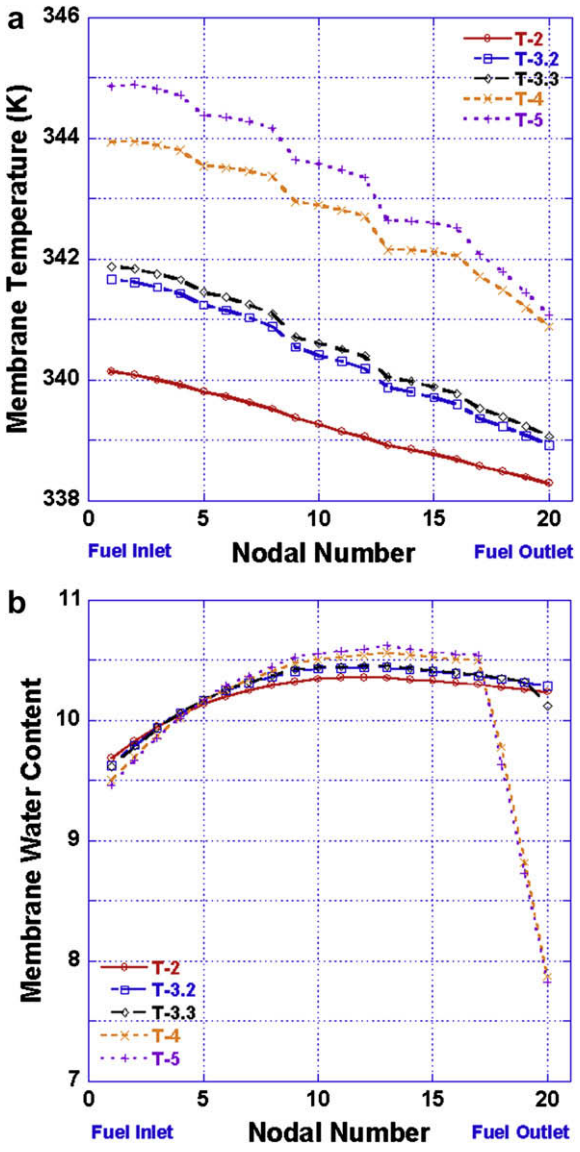

Fig. 10 – Comparisons of membrane water temperature and membrane water content along the anode channel for the type 1 configuration at a cell current density of 0.74 A/cm^2 with different coolant temperatures.

though the water diffusivity between the GDL and membrane on both sides was increased, the water activity of the anode and cathode GDLs decreased due to increased saturation pressure. This results in lower membrane water content due to decreased water flux through the membrane electrolyte. The membrane conductivity is determined by Equation 32. The first term, provided in Equation 33, is proportional to the membrane water content, and the second term, provided by Equation 34, is an exponential function of membrane temperature. Thus, the electrical resistance can be decreased by increasing either membrane water content and/or temperature. However, the membrane water content generally decreases with increasing temperature. When the temperature of the membrane is increased from 340.9 K to 341.1 K, the magnitude of the second term is increased from 1.137 to 1.138, while the magnitude of the first term is

Table 8 – Comparison of water diffusivity, water flux, and overvoltage of type 1 model with the various temperature differences between the coolant inlet and outlet of 4 K and 5 K.

Membrane temperature at the cathode inlet (K)	340.9	341.1
Total resistance (anode)	38.20	38.17
Total resistance (cathode)	38.29	38.26
Water diffusivity (m^2/s)	3.057	3.069
Anode channel-GDL	1.557e-5	1.634e-5
Anode GDL-cathode GDL (electro-osmotic)	4.676e-5	4.636e-5
Cathode GDL-anode GDL (back-diffusion)	3.119e-5	3.002e-5
Cathode GDL-channel	5.633e-5	5.709e-5
Water formation	4.076e-5	4.075e-5
Membrane water content	7.876	7.825
Conductivity (1st function)	0.0372	0.0370
Conductivity (2nd function)	1.137	1.138
Conductivity (S/m)	0.0423	0.0420
Electric resistance (ohm)	0.2009	0.2022
Ohmic overvoltage (V)	0.134	0.135
Activation overvoltage (V)	0.504	0.505

decreased from 0.0372 to 0.0370. Since the conductivity is determined by multiplying these two terms, membrane conductivity is decreased from 0.0423 to 0.0420. Eventually the ohmic overvoltage is increased by 1 mV from 0.134 V to 0.135 V. Moreover, as the membrane temperature is increased, the activation overvoltage is increased from 0.504 V to 0.505 V. In summary, when the cathode humidity is relatively low, the overvoltage of PEMFC can be increased due to increased membrane temperature, which results in lowering the performance of the PEMFC.

Table 9 illustrates the voltage and power of the type 1 configuration at different inlet anode and cathode humidity. Fig. 11 shows the comparison of temperature and membrane water content with different inlet anode and cathode humidity of 70–70% and 80–80%. When the anode and cathode inlet humidity were simultaneously increased to 70–70%, the voltage and power were also increased to 0.5609 V and 98.50 W. When the anode and cathode inlet humidity were increased further to 80–80%, the voltage and power were increased to the same 0.5611 V and 98.54 W. In the case of 70–70% inlet humidity, even if the membrane temperature at the cathode inlet was increased 0.3 K compared to the case of 60–60% inlet humidity, the 70% cathode inlet humidity was sufficient to saturate the cathode GDL. The results confirm the well established fact that higher humidity leads to better PEMFC

Table 9 – Comparison of voltage, power and pressure loss of type 1 model at the cell current density of 0.74 A/cm^2 with various humidity values.

Anode humidity (%) – Cathode Humidity (%)	60–60	70–70	80–80
Voltage (V)	0.5577	0.5609	0.5611
Generated power (W)	97.95	98.50	98.54
Pump power (W)	0.024	0.025	0.028
Net power (W)	97.926	98.475	98.512

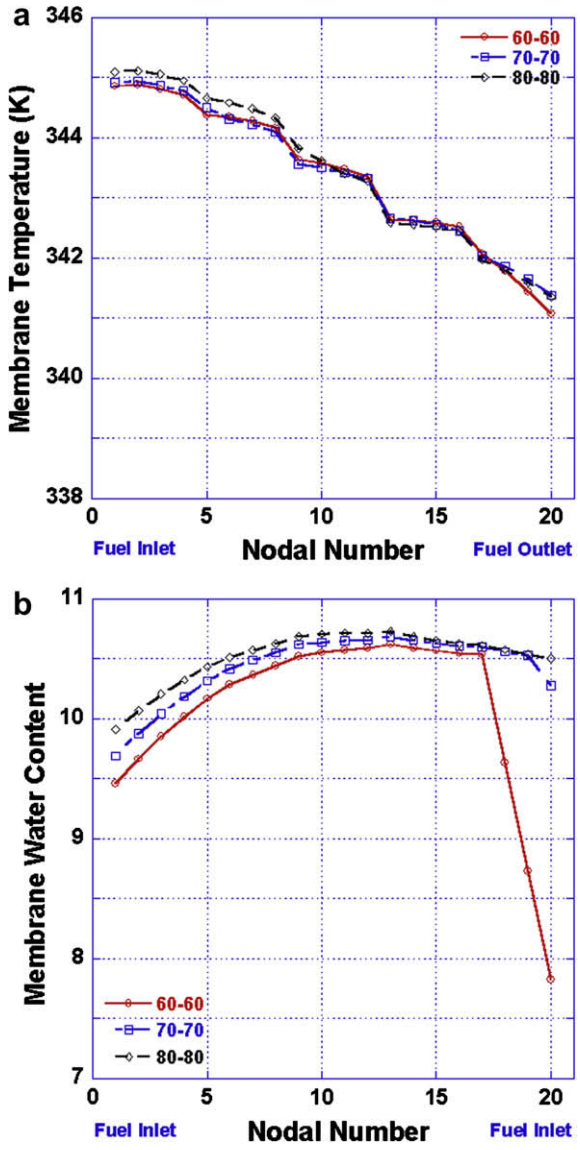

Fig. 11 – Comparisons of membrane water temperature and membrane water content along the anode channel for the type 1 model at a cell current density of 0.74 A/cm^2 with different inlet humidity levels.

performance. When the temperature difference between the coolant inlet and outlet was decreased and the inlet humidity of the anode and cathode were increased, the membrane was more hydrated, which resulted in the highest performance of the PEMFC.

4. Conclusions

The configuration effects of fuel, air, and coolant flows on the performance of a PEMFC were investigated with a reduced order dynamic model. To investigate configuration effects, quasi-three-dimensional models that have different flow types were developed. The unit cell node of each model contained the five control volumes of anode gas, anode GDL, electrolyte, cathode GDL, and cathode gas to solve the dynamic species and mass conservation equations. Seven control volumes of anode plate, anode, MEA, cathode, cathode plate, coolant, and end plate were used to solve the dynamic energy balance and to capture the details of MEA behavior including water transport.

A comparison of simulated current–voltage polarization results to experimental data shows that the PEMFC model is in good agreement with the experiment. In order to compare the performance between the five configuration types, a comparison of current–voltage and power curves was presented. While the performance of the five configurations is similar at a current density lower than 0.13 A/cm^2, the type 1 configuration has the highest performance above a current density of 0.13 A/cm^2.

In order to elucidate the factors that determine cell performance, two operating current densities – 0.74 A/cm^2 and 1 A/cm^2 – were selected and simulated. Since the inlet humidity of anode and cathode streams was relatively low, at 60–60%, the temperature of the membrane was identified as a significant factor when determining PEMFC performance. In addition, as the operating current density was increased, the cooling effect was decreased due to increasing water formation. At a current density of 0.74 A/cm^2, since the type 1 configuration has the highest degree of membrane hydration, it has the highest performance. Likewise, the type 5 configuration has the highest performance at a current density of 1 A/cm^2. However, at 1 A/cm^2, the difference between type 1 and type 5 configurations is small. Generally the performance of the type 1 configuration can be regarded as the highest over the whole range of operating current densities considered. The parasitic pump power, which is calculated in this study, was found to lack sufficient size to significantly affect the net performance of PEMFC.

The type 1 configuration was also operated with different humidity and cooling conditions to investigate the effects of humidity and cooling on the performance of the PEMFC. The PEMFC has the highest performance with the highest cooling conditions due to reduction of the saturation pressure in cathode GDL. Furthermore, it is confirmed that as the humidity of anode and cathode were increased, the performance of fuel cell improved due to increased vapor pressure in the cathode GDL.

The current model is shown to be useful for investigating the flow configuration effects of fuel, air, and coolant on the performance of PEMFC, while retaining dynamic functionality and simplicity that allow use in system models and control system development. The model can also be used to design and optimize the flow configuration and inlet conditions of PEMFC fuel, air, and coolant within a system model.

REFERENCES

[1] Ghenciu AF. Review of fuel processing catalysts for hydrogen production in PEM fuel cell systems. Curr Opin Solid State Mater Sci 2002;6(5):389–99.
[2] Mehta V, Cooper JS. Review and analysis of PEM fuel cell design and manufacturing. J Power Sources 2003;114:32–53.
[3] Costamagna P, Srinivasan S. Quantum jumps in the PEMFC science and technology from the 1960s to the Year 2000: Part I. Fundamental scientific aspects. J Power Sources 2001;102: 242–52.

[4] Springer TE, Zawodinski TA, Gottesfeld S. Polymer electrolyte fuel cell model. J Electrochem Soc 1991;136:2334.
[5] Bernardi DM, Verbrugge MW. Mathematical model of a gas diffusion electrode bonded to a polymer electrolyte. AIChE J 1991;37:1151.
[6] You L, Liu H. A parametric study of the cathode catalyst layer of PEM fuel cells using a pseudo-homogenous model. Int J Hydrogen Energy 2001;26:991–9.
[7] Burt AC, Celik IB, Gemmen RS, Smirnov AV. A numerical study of cell to cell variation in a SOFC stack. J Power Sources 2004;126:76–87.
[8] Campanari S, Iora P. Definition and sensitivity analysis of a finite volume SOFC model for a tubular cell geometry. J Power Sources 2004;132:113–26.
[9] Gurau V, Liu H, Kakac S. Two-dimensional model for proton exchange membrane fuel cells. AIChE J 1998;44:2410.
[10] Wang Y, Wang C. Transient analysis of polymer electrolyte fuel cells. Electrochim Acta 2005;50:1307–15.
[11] Um S, Wang CY. Three-dimensional analysis of transport and electrochemical reactions in polymer electrolyte fuel cells. J Power Sources 2004;125:40–51.
[12] Maher AR, Sadiq AB, Haroun AK, Shahad AJ. Parametric and optimization study of a PEM fuel cell performance using three-dimensional computational fluid dynamics model. Renew Energy 2007;32:1077–101.
[13] Sahraoui M, Kharrat C, Halouani K. Two-dimensional modeling of electrochemical and transport phenomena in the porous structures of a PEMFC. Int J Hydrogen Energy 2009;34:3091–103.
[14] Mueller F, Brouwer J, Kang S, H-Kim S, Min K. Quasi-three dimensional dynamic model of a proton exchange membrane fuel cell for system and controls development. J Power Sources 2007;163:814–29.
[15] Hontanon E, Escudero MJ, Bautista C, Garcia-Tbarra PL, Daza L. Optimisation of flow-field in polymer electrolyte membrane fuel cells using computational fluid dynamics techniques. J Power Sources 1999;86:363–8.
[16] Wang J. Pressure drop and flow distribution in parallel-channel configurations of fuel cells: U-type arrangement. Int J Hydrogen Energy 2008;33:6339–50.
[17] Arico AS, Creti P, Baglio V, Modica E, Antonucci V. Influence of flow field design on the performance of a direct methanol fuel cell. J Power Sources 2000;91:202–9.
[18] Kumar A, Reddy RG. Effect of channel dimensions and shape in the flow-field distributor on the performance of polymer electrolyte membrane fuel cells. J Power Sources 2002;113: 11–8.
[19] Soler J, Hontanon E, Daza L. Electrode Permeability and flow-field configuration influence on the performance of a PEMFC. J Power Sources 2003;118:172–8.
[20] Hu G, Fan J, Chen S, Liu Y, Chen K. Three-dimensional numerical analysis of proton exchange membrane fuel cells (PEMFCs) with conventional and interdigitated flow fields. J Power Sources 2004;136:1–9.
[21] Karvonen S, Hottinen T, Saarinen J, Himanen O. Modeling of flow field in polymer electrolyte membrane fuel cell. J Power Sources 2006;161:876–84.
[22] Lee S, Jeong H, Ahn B, Lim T, Son Y. Parametric study of the channel design at the bipolar plate in PEMFC performances. Int J Hydrogen Energy 2008;33:5691–6.
[23] Ferng YM, Su A. A three-dimensional full-cell CFD model used to investigate the effects of different flow channel designs on PEMFC performance. Int J Hydrogen Energy 2007; 32(17):4466–76.
[24] Jeon DH, Greenway S, Shimpalee S, Van Zee JW. The effect of serpentine flow-field designs on PEM fuel cell performance. Int J Hydrogen Energy 2008;33:1052–66.
[25] Jang J-H, Yan W-M, Li H-Y, Tsai W-C. Three-dimensional numerical study on cell performance and transport phenomena of PEM fuel cells with conventional flow fields. Int J Hydrogen Energy 2008;33:156–64.
[26] Freunberger SA, Santis M, Schneider IA, Wokaun A, Buchi FN. In-plane effects in large-scale PEMFCs. J Electrochem Soc 2006;153(2):A396–405.
[27] Andrew MR. Kinetic effects – Part 2. In: Williams KR, editor. An introduction to fuel cells. New York: Elsevier Publishing Company; 1966. Chapter 4.
[28] Yuyao S,Choe SY. Computation of Dehydration Effects of the Membrane in a PEM Fuel Cell. In: Proceedings of third International conference on fuel cell science, engineering and technology paper Number ASME FC2005-74163; 2005.
[29] Incropera FP, Dewitt DP. Fundamental of heat and mass transfer. New York: John Wiley and Sons; 2002.
[30] Dutta S, Shimpalee S, Van Zee J. Numerical prediction of mass-exchange between cathode and anode channels in a PEM fuel cell. Int J Heat Mass Tran 2001;44: 2029–42.
[31] White FM. Fluid mechanics. 4th ed. McGraw-Hill; 1999.